CRYSTAL GROWTH & DESIGN

Article

pubs.acs.org/crystal

Direct Nanoscale Imaging Reveals the Growth of Calcite Crystals via Amorphous Nanoparticles

Carlos Rodriguez-Navarro,*[,†] Alejandro Burgos Cara,[†] Kerstin Elert,[†] Christine V. Putnis,[‡,§] and Encarnacion Ruiz-Agudo[†]

[†]Dpto. Mineralogía y Petrología, Universidad de Granada, Fuentenueva s/n, 18071 Granada, Spain

[‡]Institut für Mineralogie, Universität Münster, 48149 Münster, Germany

[§]Nanochemistry Research Institute, Curtin University, Perth, Western Australia 6845 Australia

Supporting Information

ABSTRACT: The formation of calcite ($CaCO_3$), the most abundant carbonate mineral on Earth and a common biomineral, has been the focus of numerous studies. While recent research underlines the importance of nonclassical crystallization pathways involving amorphous precursors, direct evidence is lacking regarding the actual mechanism of calcite growth via an amorphous phase. Here we show, using *in situ* atomic force microscopy and complementary techniques, that faceted calcite can grow via a nonclassical particle-mediated colloidal crystal growth mechanism that at the nanoscale mirrors classical ion-mediated growth, and involves a layer-by-layer attachment of amorphous calcium carbonate (ACC) nanoparticles, followed by their restructuring and fusion with the calcite substrate in perfect crystallographic registry. The ACC-to-calcite transformation occurs by an interface-coupled dissolution−reprecipitation mechanism and obliterates or preserves the nanogranular texture of the colloidal growth layer in the absence or presence of organic (macro)molecules, respectively. These results show that, in addition to classical ion-mediated crystal growth, a particle-mediated growth mechanism involving colloidal epitaxy may operate in the case of an inorganic crystal such as calcite. The gained knowledge may shed light on the mechanism of $CaCO_3$ biomineralization, and should open new ways for the rational design of novel biomimetic functional nanomaterials.

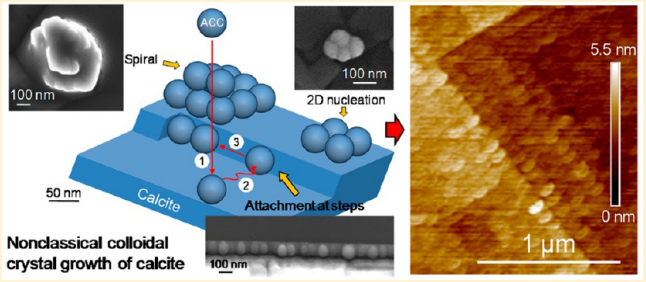

INTRODUCTION

Crystallization from solution is a fundamental process for the formation of structurally ordered solid phases such as minerals and biominerals, or novel functional materials and drugs.[1−3] According to classical crystallization theory, it starts with the spontaneous clustering of ions/molecules (i.e., monomers) leading to nucleation once a free energy barrier is overcome for a critical cluster size; afterward, such clusters grow by incorporation of ions/molecules resulting in the formation of (faceted) crystals, and minimizing the system free energy.[1,3] However, experimental and theoretical studies have recently challenged this view.[3−8] In the case of the $CaCO_3$−H_2O system, which has been the subject of extensive research due to its technological and scientific relevance,[2−5] in addition to classical ion-mediated nucleation and crystal growth,[2−4] nonclassical nucleation involving the formation of (meta)stable prenucleation clusters (PNCs) and their aggregation into solid ACC,[6] with or without the formation of dense liquid precursors,[7,8] has been reported. Interestingly, formation of calcium carbonate biominerals via ACC precursors appears to be a general biomineralization strategy[9−12] that could be mimicked by materials chemists to synthesize novel functional materials.[8] Nonclassical crystal growth involving the oriented attachment of (nano)crystalline particles, in some cases forming "mesocrystals", has also been reported.[3,13] Moreover, recent studies suggest that a particle-mediated growth involving ACC nanoparticles stabilized by organic macromolecules[14] may help explain the origins of the commonly observed nanogranular features of biomimetic[15,16] and biotic calcite (and aragonite)[14,17] (Figure S1). These particle-mediated growth mechanisms are in stark contrast to classical crystallization theory, that postulates that crystal growth in solution is a layer-by-layer process that takes place by step generation and spreading (via ions/molecules incorporation at kink sites), either at emerging dislocations or after 2-dimensional (2D) and/or 3D surface nucleation (i.e., terrace-ledge-kink -TLK- model).[1,3,18,19] The recent progress in the understanding of biotic and biomimetic calcium carbonate crystallization points to the coexistence of both classical ion-mediated and nonclassical (nano)particle-mediated growth mechanisms.[3,14] However, fundamental knowledge is still lacking regarding the involvement of ACC in crystalline $CaCO_3$ growth.[3] In particular, there is no direct *in*

Received: August 17, 2015
Revised: February 12, 2016
Published: February 23, 2016

DOI: 10.1021/acs.cgd.5b01180
Cryst. Growth Des. 2016, 16, 1850−1860

situ evidence revealing what is the exact mechanism of calcite crystal growth via an amorphous nanoparticle precursor.

Here we reveal a nonclassical particle-mediated colloidal growth mechanism for crystalline calcite via an amorphous precursor phase. Using direct observations from *in situ* atomic force microscopy (AFM) of the growth of calcite crystals, we present results of crystal growth from solutions at room *T*, both with and without an organic additive, poly(acrylic acid) (PAA), commonly used for biomimetic calcite crystallization[20] (see Methods section). We present the first direct nanoscale evidence showing that, in addition to classical crystal growth via incorporation of ions at growth steps, faceted calcite crystals can grow nonclassically by a layer-by-layer process involving the attachment of ACC nanoparticles at the calcite−solution interface followed by their amorphous-to-crystalline transformation and fusion with the underlying calcite substrate. Under our experimental conditions, this particle-mediated crystal growth mechanism operates both in the presence and in the absence of an organic additive. However, only in the presence of the organic (macro)molecules are the nanogranular features indicative of such a nonclassical crystal growth mechanism retained.

RESULTS

In situ AFM experiments show that, for supersaturation, $\sigma_{calcite}$ ($\sigma = \ln(IAP/k_{sp})$, where IAP is the ion activity product, and k_{sp} is the solubility product of the relevant phase)[19] up to 4.81, corresponding to the solubility of ACC,[21] a classical stepwise layer-by-layer growth of calcite occurs (Figure S2). For $\sigma_{calcite} \geq$ 4.81 massive nucleation of ACC particles occurs within the injection system of the AFM fluid cell. Such particles interfere with the image acquisition. A similar effect is observed upon injection of aqueous dispersions of ACC nanoparticles. To bypass this critical problem we induced the direct formation of ACC nanoparticles within the AFM fluid cell by injecting a saturated $Ca(OH)_2$ solution (15.7 mM free $[Ca^{2+}]$, see Methods section). In contact with this solution that is undersaturated with respect to calcite, dissolution of $\{10.4\}_{calcite}$ surfaces occurs until supersaturation with respect to ACC is reached within a thin fluid layer at the calcite interface (thickness ≤12 μm) (see modeling of σ_{ACC} evolution in Methods section, and Figure 1). This leads to the precipitation of ACC nanoparticles (confirmed by *ex situ* analyses, see below) in less than 3−5 s, and their attachment onto $(10.4)_{calcite}$ (Figure 2a). These nanoparticles display a flattened geometry (width = 62 ± 13 nm, height = 37 ± 2 nm), which suggests that the nascent ACC nanoparticles have a liquid-like character that leads to their flattening upon surface attachment.[22] ACC nanoparticles eventually cover the entire calcite surface, morphing nanofeatures, such as etch pits and step edges, of the substrate (Figure 2a). ACC nanoparticles grow at an initial rate, *R*, of 11 ± 3 nm/s, similar to that reported for ACC formed at a calculated $\sigma_{ACC} = 1$ ($\sigma_{calcite} = 5.81$),[23] that decreases ($R \rightarrow 0$ nm/s) as the system approaches equilibrium (saturation with respect to ACC) (Figure 2b). After ca. 22−30 min, ACC nanoparticles acquire rhombohedral features typical of calcite growth islands due to dissolution of ACC coupled with crystallization and further classical (layer) growth of calcite (Figure 2c and Figure S3).

Ex situ analyses (see Methods section and Figures S4−S7) confirm that ACC nanoparticles are the building units of the calcite overgrowth observed in AFM. TEM images (Figure 2d,e and Figure S5) and STEM-EDS analysis (Figure S6) show that

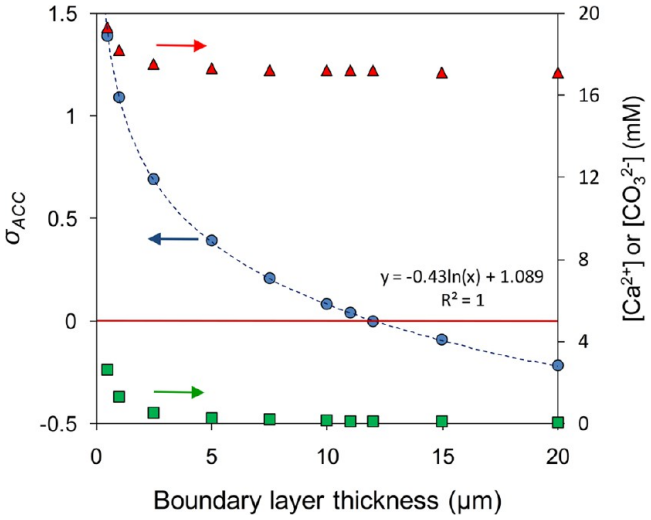

Figure 1. Supersaturation vs boundary layer thickness. Calculated dependence between supersaturation with respect to ACC ($k_{sp} = 10^{-6.39}$), σ_{ACC} vs boundary layer thickness at the calcite−solution interface where CO_3^{2-} and Ca^{2+} ions diffuse toward the bulk solution after calcite dissolution upon contact with the saturated $Ca(OH)_2$ solution (values follow a logarithmic trend, dashed blue line). The red horizontal line marks saturation with respect to ACC (i.e., $\sigma_{ACC} > 0$ indicates supersaturation with respect to ACC). The free calcium (red triangles) and free carbonate (green squares) concentrations (calculated using PHREEQC) are also plotted.

the ca. 40 ± 10 nm surface overgrowth is initially ACC (up to 2 min reaction time in $Ca(OH)_2$ solution) and after 22 min transforms into a mosaic-like aggregate of calcite nanocrystals, overgrown in crystallographic continuity with the calcite substrate (Figure 2f,g). In air, transformation into calcite readily occurs in a humid environment (85% RH), but not in a dry environment, suggesting that under our experimental conditions (72 h humid air exposure) a dissolution−reprecipitation mechanism is responsible for the ACC-to-crystalline conversion,[8] consistent with AFM results (Figure 2c and Figure S3). FESEM imaging also shows aggregated ACC nanoparticles ca. 30−80 nm in diameter at 2 min reaction time, forming continuous layers on $(10.4)_{calcite}$ surfaces, limited by macrosteps (ca. 40−80 nm high) (Figure 2h,i). ACC nanoparticles then merge rendering continuous, flat terraces (i.e., $(10.4)_{calcite}$) limited by rough macrosteps (Figure 2j). In some areas, individual ACC nanoparticles are observed on top of the ACC overgrowth (Figure 2h), while in other areas multilayer ACC overgrowths are detected (Figure S8).

N_2 adsorption isotherms show that the surface area of calcite (0.5 ± 0.1 m^2/g) increases (5 ± 1 m^2/g) when ACC forms, and then decreases (2 ± 0.2 m^2/g) when it transforms into calcite (Figure 3). This is also observed in experiments when PAA was added (see below). Concurrent with the initial surface area increase, our thermogravimetry/differential scanning calorimetry (TG/DSC) analyses show that solids reacted for 2 min display a weight loss step in the 100−300 °C range (loss of H_2O; very rapid up to ∼200 °C, then very slow and minimal up to ∼300 °C), a feature consistent with the presence of small quantities of (hydrated) ACC on the calcitic substrate (which decarbonates, endothermal peak in DSC, at $T > 600$ °C) (Figure S7).[8,11] In contrast, samples that reacted for longer periods of time (22 min), thus displaying a reduction in surface area, show no weight loss due to dehydration. These results are

DOI: 10.1021/acs.cgd.5b01180
Cryst. Growth Des. 2016, 16, 1850−1860

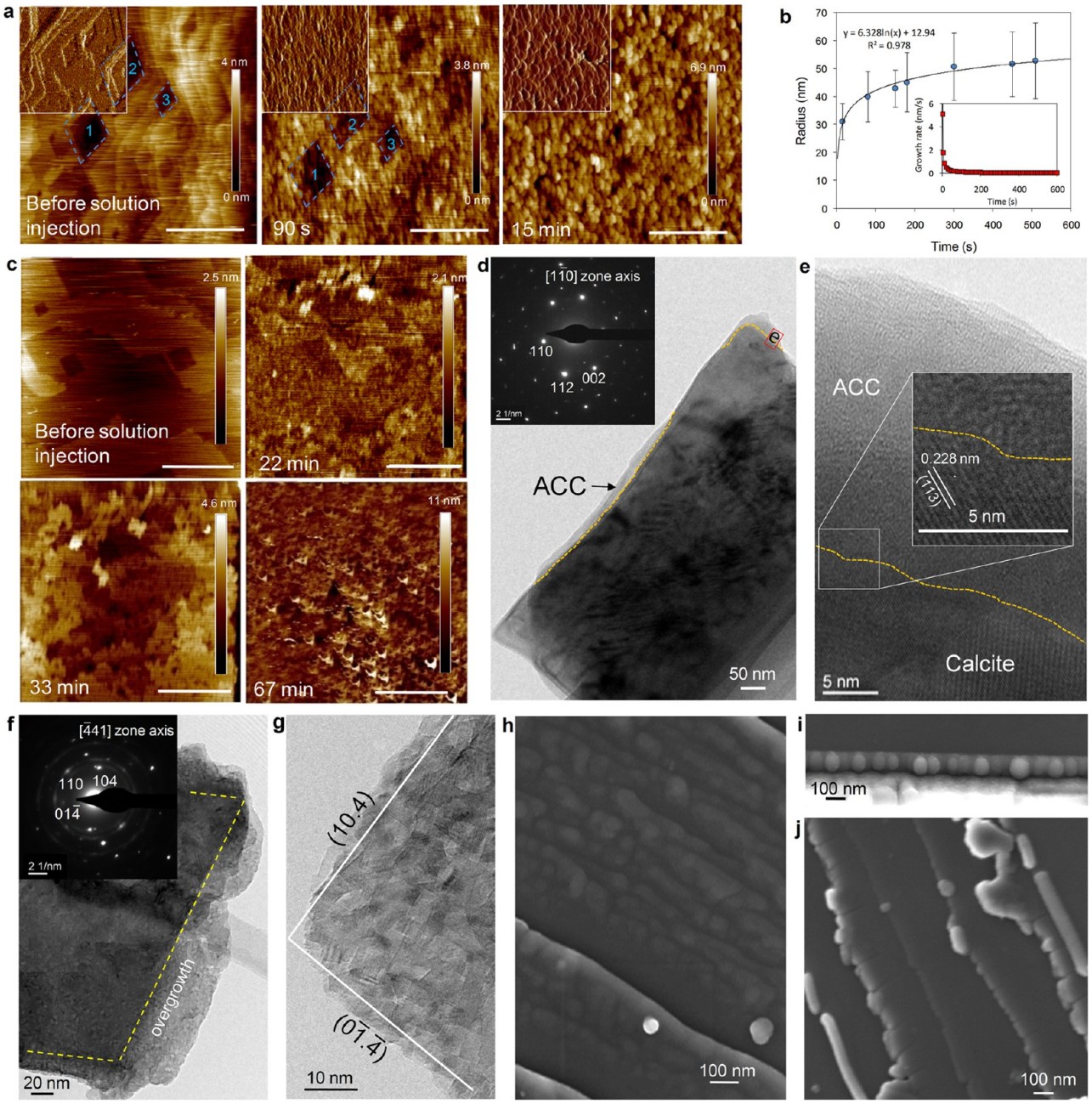

Figure 2. Calcite growth via attachment of ACC nanoparticles. (a) AFM snapshots (height images) of the initial deposition of ACC nanoparticles on $(10.4)_{calcite}$ and their subsequent growth. Insets: deflection image of squared areas. Note that the slightly ellipsoidal geometry of the nanoparticles is due to sample drifting during image acquisition (consistent with the parallel elongation of all nanoparticles). Blue dashed lines mark the contour of three (1, 2, and 3) dissolution pits in sequential AFM images. (b) Evolution of ACC particle size vs *t*. Growth rates vs *t* in inset. (c) AFM height images of ACC layer formation (0−22 min), restructuring and transforming into calcite growth islands (22−33 min), and final growth and polygonization (67 min). Scale bars in parts a and c: 1 μm. (d) TEM image of an ACC overgrowth on calcite after 2 min contact with $Ca(OH)_2$ solution. SAED pattern in inset. (e) HRTEM image of red squared area in part d showing $(113)_{calcite}$ lattice fringes and the ACC overgrowth. Detail of the white squared area in inset. (f) Oriented crystalline overgrowth after 22 min in contact with $Ca(OH)_2$ solution (SAED pattern in inset: the spotted Debye rings correspond to CaO formed after e-beam induced, topotactic calcite decomposition). (g) Detail of the overgrowth (calcite with mosaic texture). FESEM top view (h) and lateral view (i) of nanogranular ACC (2 min reaction), and flattened features (j) following ACC to calcite transformation (22 min reaction time).

consistent with TEM-SAED observations showing that the initial (hydrated) ACC transforms into an anhydrous crystalline $CaCO_3$ (i.e., calcite) over time when in contact with the solution.

Dissolution of the ACC surface layer in deionized water (see Methods section for a detailed description of *in situ* AFM dissolution experiments) is anisotropic, progressing via pit formation and spreading, leaving a retreating constant height (ca. 40 nm) dissolution front (Figure 4). Note, however, that the rhombohedral etch pits of the calcite substrate do not spread as the dissolution of the overgrowth progresses (Figure 4b). These results confirm that the overgrowth is indeed ACC (i.e., more soluble than calcite)[21] and suggest that upon

DOI: 10.1021/acs.cgd.5b01180
Cryst. Growth Des. 2016, 16, 1850−1860

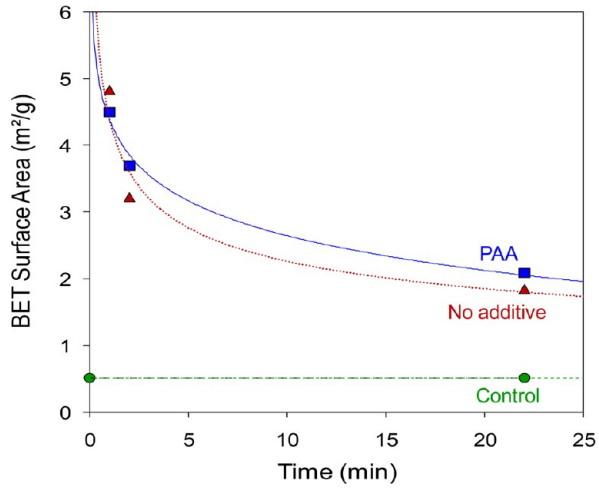

Figure 3. BET surface area evolution of calcite crystals. Control: calcite exposed to DI water. No additive: calcite subjected to ACC-mediated growth in an additive-free $Ca(OH)_2$ saturated solution. PAA: calcite subjected to ACC-mediated growth in a $Ca(OH)_2$ saturated solution dosed with 60 μg/mL PAA. Note the reduction in surface area as reaction time increases (experimental results are fitted to a ln function), but does not reach the initial low values of the calcite control (within the experimental time-span).

attachment onto calcite ACC nanoparticles undergo a structural rearrangement that renders them anisotropic.

Similar *in situ* AFM (Figure 5) and *ex situ* results (Figure 3 and Figures S9 and S10) are obtained following calcite growth in the presence of a saturated $Ca(OH)_2$ solution dosed with 60 μg/mL PAA. However, the nanocluster morphology of the original ACC overgrowth is preserved after the amorphous-to-crystalline transformation (Figure S10). In the presence of PAA, the ACC nanoparticles attach onto the calcite substrate in an aligned way (close-packing), as shown by AFM imaging (Figure 5). Apparently, PAA not only stabilizes ACC nanoparticles,[20] but also seems to facilitate their ordered alignment on the calcite surface (i.e., what appears to be an assisted self-assembly). Sequential AFM images show that ACC particles can attach on (see paired white and orange circles in Figure 5) or detach from (or diffuse on the surface of) the calcite surface (see paired green circles in Figure 5). This shows that ACC nanoparticles do not directly precipitate on the calcite surface, but rather, they form in solution and diffuse to the calcite surface where they attach (or detach) in an ordered, aligned way.

To test if the observed growth mechanism was exclusive to our system, dispersion droplets of ACC nanoparticles (with size 50 ± 20 nm) were deposited onto freshly cleaved $(10.4)_{calcite}$ crystals or calcite powders (see details in Methods section, and Figure S11 that shows the characteristics of ACC nanoparticles). FESEM imaging shows that ACC nanoparticles attach onto calcite along specific crystallographic directions forming (multiple) monolayers limited by rough macrosteps ca. 50 nm high (Figure 6a,b). It is important to note that the deposition onto the calcite substrate of ACC nanoparticles in

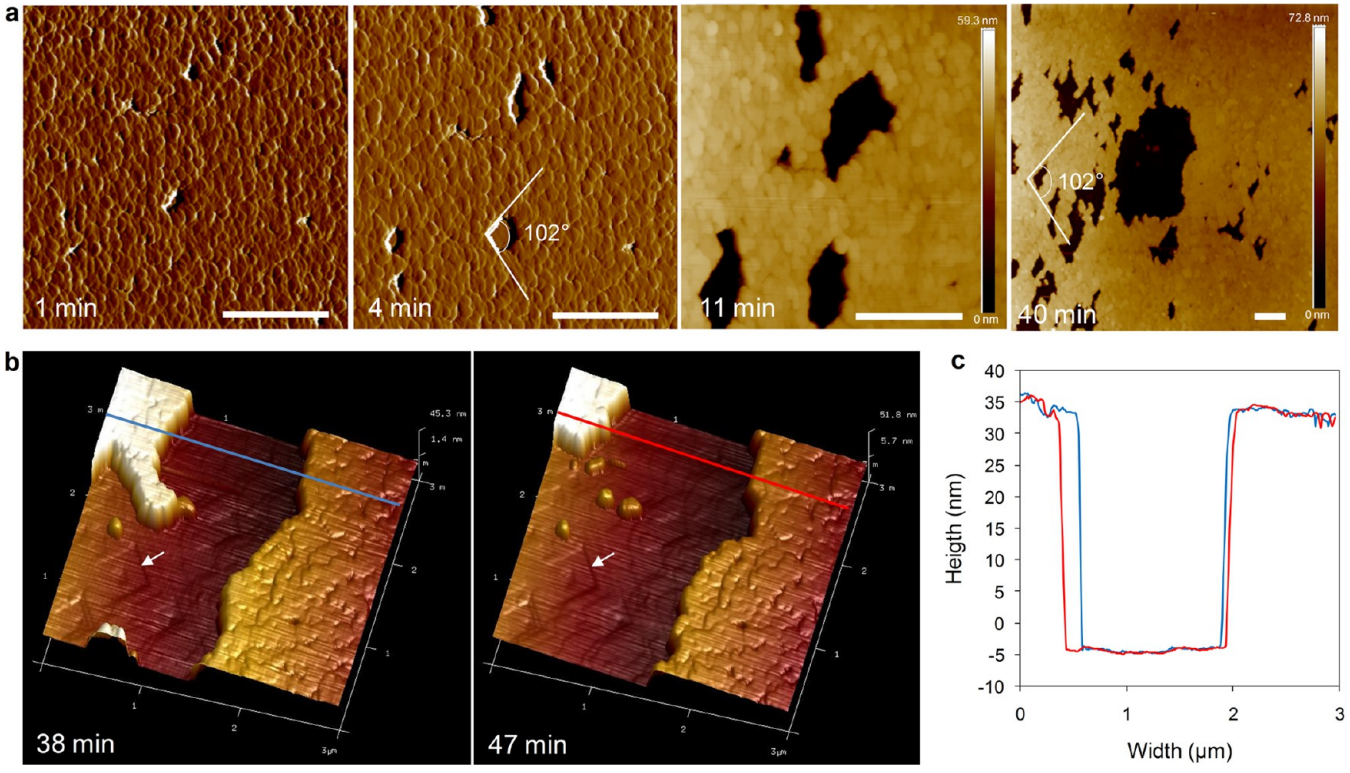

Figure 4. AFM snapshots of ACC dissolution following water injection into the fluid cell. (a) Evolution of the dissolution of the ACC overgrowth developed onto $(10.4)_{calcite}$ (1 and 4 min after water injection, deflection images; 11 and 40 min after water injection, height images). Some dissolution pits display ledges parallel to $\langle\bar{4}41\rangle$ calcite (obtuse angles of 102°). Scale bars: 1 μm. (b) 3D height images showing the advancement of the dissolution front in directions parallel to the underlying $(10.4)_{calcite}$ substrate. No step retreat is observed in rhombohedral pits already present in the calcite substrate before ACC attachment (arrows). (c) Height profiles along the blue and red lines in part b showing the advancement of the constant-height dissolution front.

DOI: 10.1021/acs.cgd.5b01180
Cryst. Growth Des. 2016, 16, 1850−1860

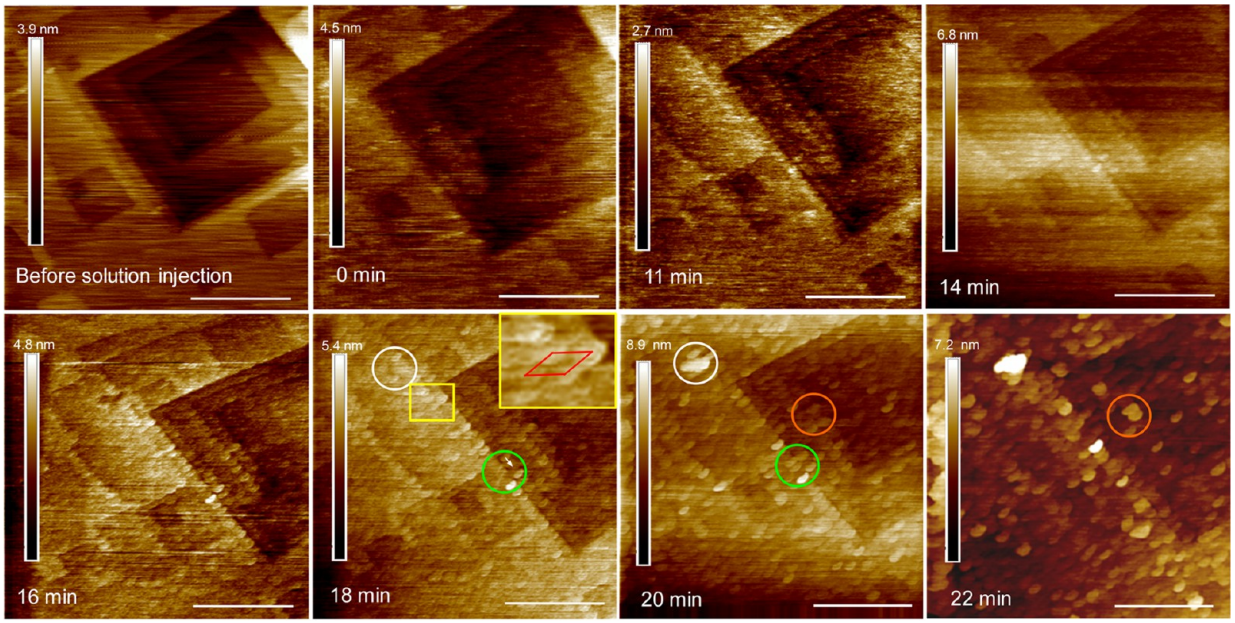

Figure 5. Sequential AFM height images of the attachment on $(10.4)_{calcite}$ and growth of ACC nanoparticles formed upon contact of the calcite surface with the $Ca(OH)_2$ solution dosed with 60 μg/mL PAA. Note the precise alignment of ACC nanoparticles along step edges of the dissolution pits already present on the calcite substrate before solution injection. Solution injected at t = 0 min. The paired white and orange circles mark areas where ACC nanoparticles attach, while the paired green circles mark an area where an ACC nanoparticle detaches/moves (white arrow). The inset in the image collected after 18 min is a magnified view of the yellow squared area. The red polygon in the inset marks what resembles an ACC hexagonal close-packed unit cell. Note that the slightly ellipsoidal geometry of the nanoparticles is due to sample drifting during image acquisition (consistent with the parallel elongation of all nanoparticles). Scale bar: 1 μm.

the aqueous dispersion should, in principle, be a stochastic process. As such, a random distribution of nanoparticles (or aggregates) on such a substrate should be achieved.[24] However, FESEM observations do not show this (Figure 6a,b). Indeed, the ACC overgrowth is formed by multilayers limited by flat terraces, generally free of surface ACC nanoparticles (see details in Figure 6b). This implies that the nanoparticles that deposit onto each terrace have to undergo surface diffusion until they finally attach to a macrostep, thereby leaving an almost clean terrace. Because this process is frozen upon sample collection for analysis, a few ACC nanoparticles could not reach the macrosteps, so they can be observed as isolated nanoparticles on some terraces (Figure 6a,b).

In some cases structures which resemble macrospirals of ACC nanoparticles are observed on $(10.4)_{calcite}$ surfaces (Figure 6c and Figure S12). These structures are reminiscent of the macrospirals observed in some biominerals (Figure S1). AFM reveals the globular nanocluster morphology of the overgrowth (Figure 6d and Figure S13). Upon 72 h aging at 85% RH, transformation into smooth calcite overgrowths on $(10.4)_{calcite}$ occurs (Figure 6e). TEM analyses confirm the overgrowth is composed of ACC nanoparticles (Figure 6f,g), that upon exposure to humid air transform into calcite, preserving the orientation and morphology of the calcite substrate (Figure 6h). Similar experiments in which ACC nanoparticles were synthesized in the presence of 60 μg/mL PAA show that this organic additive facilitates the preservation of the original nanocluster morphology after the ACC-to-calcite transformation (Figures S14–S16).

DISCUSSION

Overall, our results show that formation (at high supersaturation) and attachment of ACC nanoparticles is a viable nonclassical crystal growth mechanism for faceted calcite crystals. This challenges the current understanding of crystal growth in solution[25] and mirrors at the nanoscale classical ion-mediated crystal growth[18,19] (Figure 7a,b). Growth can take place via ACC nanoparticle attachment involving surface diffusion and final incorporation (concurrent with dehydration/restructuring) at macrosteps, resulting from previously attached ACC particles that form 2D islands and/or macrospirals on the calcite surface (Figure 7c).

In the case of the *in situ* experiments involving injection of a saturated $Ca(OH)_2$ solution into an AFM fluid cell, it was unexpected to observe the formation of ACC nanoparticles, as opposed to the thermodynamically more favorable (exothermic) (re)growth of the calcite substrate via (classical) incorporation of Ca^{2+} and CO_3^{2-} ions. Considering that the initial ACC nanoparticles displayed a liquid-like character, we suggest that ACC formation is kinetically favored, as opposed to classical crystal growth, because once the system is sufficiently supersaturated, it can undergo a liquid–liquid spinodal decomposition[8] (with no free energy barrier).[3] However, further detailed analyses are needed (for instance, using *in situ* liquid cell TEM)[4] to confirm this hypothesis. Alternatively, it could be argued that ACC could directly nucleate onto the calcite substrate (i.e., heterogeneous nucleation). This possibility, however, is not consistent with our AFM and FESEM observations (e.g., individual ACC nanoparticles on top of an ACC layer, or ACC multilayers). It is also not consistent with Pouget et al.'s[5] cryo-TEM observations showing the formation of ACC nanoparticles (~30 nm in size) in the bulk solution near a template (stearic acid monolayer) and their subsequent attachment to such a template, where they finally converted into oriented crystalline $CaCO_3$. These observations demonstrate that ACC nano-

DOI: 10.1021/acs.cgd.5b01180
Cryst. Growth Des. 2016, 16, 1850–1860

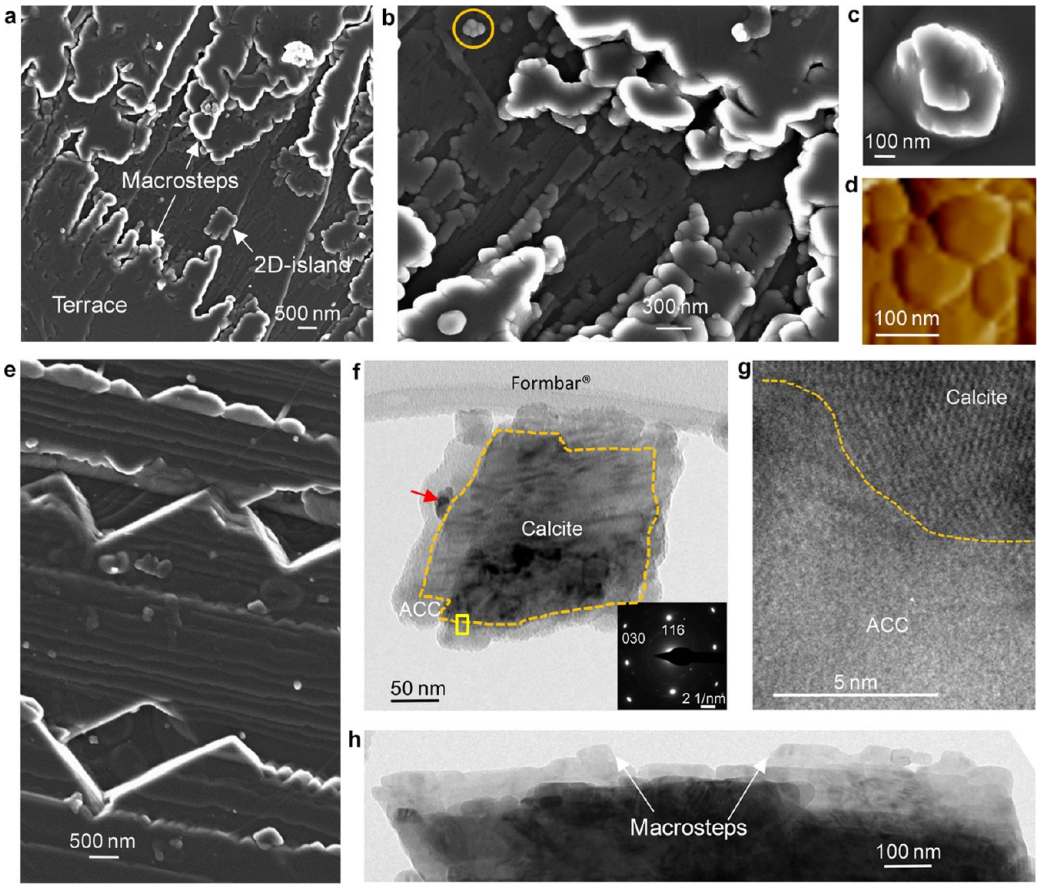

Figure 6. Calcite growth after supply of ACC nanoparticle dispersions. (a) FESEM micrograph of growth layers (terraces) limited by rough macrosteps formed by ACC nanoparticles. (b) Detail of fused ACC nanoparticles at macrosteps/terraces and 2D islands made up of ACC clusters (circle). (c) Detail of what resembles a macrospiral of ACC nanoparticles on $(10.4)_{calcite}$. The seemingly rhombohedral contour suggests that some degree of ACC-to-calcite transformation has already taken place. (d) Representative AFM (deflection) image of ACC clusters on calcite. (e) Same as parts a and b after 72 h at 85% RH. The nanogranular features in macrosteps/terraces disappear after ACC-to-calcite transformation via dissolution−precipitation. (f) TEM photomicrograph of calcite with an ACC overgrowth (marked by the dashed line). Incipient ACC-to-calcite transformation is detected (red arrow) ($[\bar{1}00]$ zone axis SAED pattern in inset). Note that BET surface area measurements show that the ACC overgrowth is porous. This enables water to access the interior of the overgrowth thus triggering the ACC-to-calcite transformation. (g) HRTEM image showing the ACC−calcite interface (inset area in part f). (h) TEM image of calcite with an ACC overgrowth transformed into syntaxial calcite after 72 h in humid air. Note the macrosteps resulting from the initial ACC layer-by-layer growth.

particles can form in the bulk solution and later on attach to a substrate, as observed here.

Our observations suggest that the formation of the ACC overgrowths must involve nanoparticle surface diffusion and attachment at kinks present at macrosteps (formed after 2D surface nucleation and/or macrospiral growth) to preserve the overall shape of the crystal substrate bounded by specific (*hkl*) faces observed here; otherwise, simple agglomeration/sedimentation of nanoparticles would be observed. Such a particle-mediated layer-by-layer growth involving macrosteps is strikingly similar to that observed in epitaxial growth of colloid crystals.[26] As in the latter case, the template effect of the (crystalline calcite) substrate appears to be critical for the layer-by-layer colloidal crystal growth via the attachment of ACC nanoparticles. In fact, control experiments in which ACC nanoparticle dispersion droplets were deposited onto non-crystalline substrates (silica glass slides) result in the random sedimentation of ACC nanoparticle aggregates (Figure S17a). Moreover, similar control experiments in which the substrate was crystalline, but not calcite (ultraclean [100]-oriented silicon wafer and quartz substrates), also result in the random deposition of aggregates made up of ACC nanoparticles (Figures S17b,c). These results confirm that the template effect of the calcite structure is required for the observed layer-by-layer nanoparticle-mediated growth. Apparently, the influence of the calcite substrate can induce the attachment of ACC nanoparticles along specific crystallographic directions. It could be argued that this is due to the existence of steps on the $(10.4)_{calcite}$ surface. Such steps could act as physical barriers enabling the alignment of ACC nanoparticles undergoing surface diffusion. However, our AFM measurements show that steps on $(10.4)_{calcite}$ are typically ~0.3 nm in height (Figure 2a,c). It is thus difficult to imagine how such steps can be a barrier for ACC nanoparticles with diameters almost 3 orders of magnitude larger (~40−80 nm). Conversely, it could be argued that the (electrostatic) field emerging from the calcite substrate[27] could enable the oriented attachment of ACC nanoparticles. However, because ACC nanoparticles are amorphous (i.e., they lack long-range order) they should not undergo an "anisotropic" (oriented) attachment onto a crystalline template (i.e., calcite). It has been recently proposed that oriented attachment of poorly crystalline or even amorphous nanoparticles can take place provided that there is a surrounding field that promotes particles to adopt favorable

DOI: 10.1021/acs.cgd.5b01180
Cryst. Growth Des. 2016, 16, 1850−1860

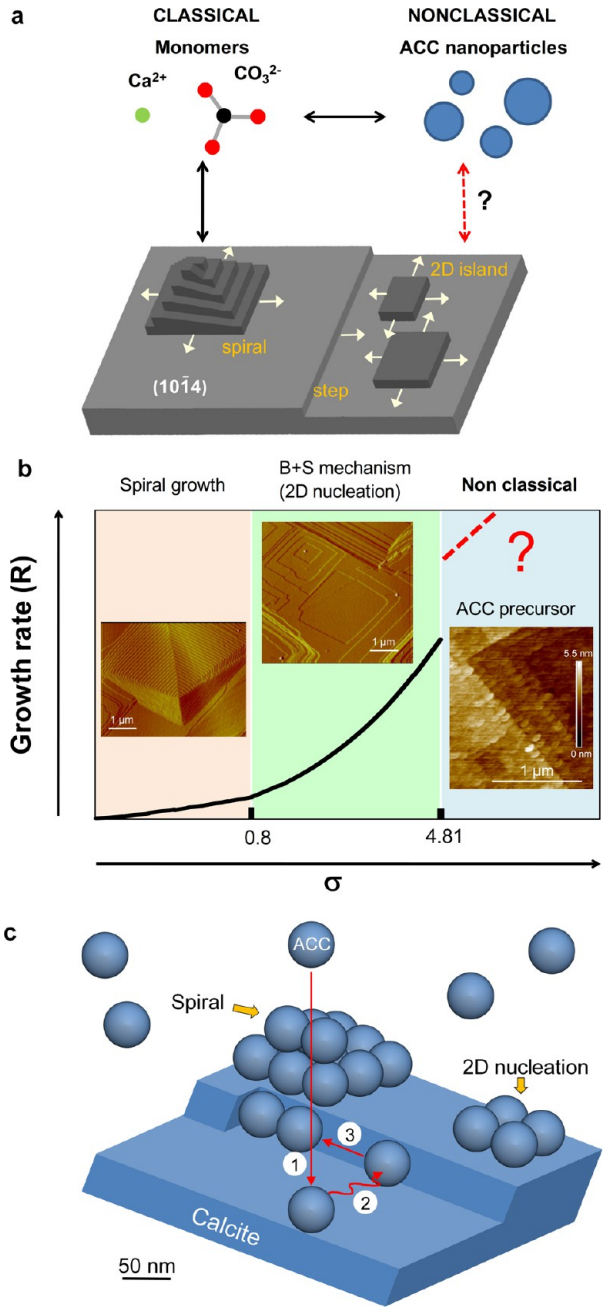

Figure 7. ACC nanoparticle precursors and calcite crystal growth. (a) Classical and nonclassical pathways for calcite growth. (b) Calcite growth mechanisms and rates, R vs supersaturation, $\sigma_{calcite}$. Insets show *in situ* AFM deflection images of spiral growth and 2D surface nucleation and growth (birth-and-spread, B + S, model), and a height image of calcite growth via ACC attachment along steps according to the proposed nonclassical mechanism of particle-mediated growth from a colloidal dispersion at the calcite−solution interface. (c) Diagram showing spiral growth and 2D nucleation of ACC nanoparticles on $(10.4)_{calcite}$. Growth involves ACC nanoparticle bulk diffusion (1), surface diffusion (2), and final diffusion/attachment to a kink (3) where restructuring and fusion with the calcite substrate occurs.

configurations prior to the attachment step.[28] This can be achieved if ACC nanoparticles adopt a short- or medium-range order (e.g., calcitic protostructure),[29] enabling their attachment onto calcite along specific [*hkl*] directions (forming macrosteps), and resulting in the observed layer-by-layer growth (as well as in the anisotropic dissolution features of the ACC overgrowth observed by means of AFM). Note that we have previously shown that ACC nanoparticles with calcitic medium-range order can undergo oriented attachments forming 1D and 2D structures in the bulk solution (i.e., a direction-specific anisotropic particle assembly process).[8] We suggest that once a first layer of ACC transforms into calcite, the aforementioned template effect could operate in the case of a second ACC layer, and so on, thus enabling the layer-by-layer growth of calcite via ACC nanoparticle attachment to continue. This mechanism can apply when ACC nanoparticles are formed *in situ* (AFM experiments) or elsewhere, and are supplied as a dispersion to the calcite substrate.

Our results also show that once an ACC overgrowth is formed, in contact with the solution, a significant restructuring takes place following transformation of ACC into calcite, both in the absence and presence of PAA. This is supported by the significant surface area reduction observed following ACC-to-calcite conversion. It is interesting to point out that a similar surface area reduction has been reported following aging of calcite "mesocrystals", formed via an ACC precursor.[30] Also, several calcite biominerals known to form via an amorphous precursor, such as sea urchin spicules, display a very low surface area (0.8−2.4 m^2/g), consistent with the hypothesis that biominerals tend to be "space filling".[31] Our results suggest that such a "space filling" ability could be achieved after ACC-to-calcite transformation via a dissolution−reprecipitation mechanism.

Ultimately, we show that calcite crystal growth can proceed via both classical (ion incorporation) and nonclassical (nanoparticle attachment) routes, dependent on supersaturation (Figure 7b). Remarkably, both growth processes follow the same spiral and 2D nucleation processes, despite the order of magnitude differences in size between building units (ions vs nanoparticles). Our results suggest that the commonly observed nanogranular morphology of $CaCO_3$ biominerals,[14,17] and their biomimetic counterparts[2,13,15,16,20] may result from colloidal crystal growth via attachment of ACC nanoparticles onto a crystalline $CaCO_3$ substrate. However, such nanofeatures are only preserved upon ACC-to-calcite conversion if organic molecules are present (e.g., PAA). We suggest that this occurs because the transformation of ACC-to-calcite can take place via an interface-coupled dissolution−precipitation mechanism.[32] This mechanism, that involves an interfacial fluid between parent and product phases, and the coupling between the dissolution of the parent phase and the precipitation of the product phase, typically leads to pseudomorphic features.[8,32,33] Note that if full dissolution followed by (nonspatially related) precipitation would have taken place, a pseudomorphic replacement of ACC by calcite, preserving the nanogranular features of the original ACC growth layer, would not have occurred. However, such a pseudomorphism, resulting in the observed nanogranular features, is only preserved when PAA is present. In the absence of PAA, calcite can continue to growth (via a classical stepwise growth, as shown by our AFM experiments) after the ACC-to-calcite transformation, thereby losing all the nanogranular features of ACC. Such a continuous growth does not occur when PAA is present. This is likely to be due to the accumulation of the organic molecules around the nanoparticles after the ACC-to-calcite transformation (i.e., a classical process of "purification" through (re)crystallization),[34] that can

DOI: 10.1021/acs.cgd.5b01180
Cryst. Growth Des. 2016, 16, 1850−1860

passivate the calcite nanoparticles preventing their regrowth. This hypothesis, however, requires further study.

Particle-mediated growth involving a colloidal amorphous phase possesses several advantages,[8] including the efficient and fast supply of material with minimal amounts of solvent. This is an energy-efficient mechanism leading to fast growth, as commonly occurs in biominerals formed via ACC (e.g., calcitic egg shells grow via ACC at a rate of up to ~10 nm s^{-1}, while inorganic calcite typically grows at rates orders of magnitude lower).[35] We suggest that the results reported here show a novel nonclassical crystal growth mechanism from a colloidal dispersion at the calcite−solution interface, involving amorphous nanoparticle attachment and restructuring. We speculate that this is a possible growth mechanism that may operate in many biomineralization systems (including the $CaPO_4$−H_2O system)[36] and their synthetic counterparts, and in other mineral systems as recent experimental results suggest.[37]

The gained knowledge of the growth of crystalline phases via amorphous nanoparticle precursors could lead to the rational design and colloidal synthesis (likely involving colloidal epitaxy) of novel biomimetic materials with a range of applications (e.g., biomaterials and photonic crystals). It may also have implications for the better understanding of calcite growth in nature (e.g., biomineralization) and in relevant technological scenarios such as mineral CO_2 sequestration.

METHODS

Growth Solution and Calcite Crystals. Saturated solutions were prepared by dissolving $Ca(OH)_2$ crystals in double-deionized Milli-Q water (resistivity > 18 mΩ) in a sealed plastic bottle with no head space (to prevent dissolution of atmospheric CO_2). Vacuum-filtered clear saturated solutions with no dispersed solids (i.e., no Tyndall effect) were used during calcite growth experiments. Saturated $Ca(OH)_2$ solutions (pH 12.4, 20 mM total calcium, 15.73 mM free calcium-calculated using PHREEQC, see below) were either pure or dosed with 60 μg/mL poly(acrylic acid) (PAA, sodium salt, mw, 2300; Sigma-Aldrich). Optical quality calcite crystals (Chihuahua, Mexico) ca. 3 × 4 × 1 mm^3 in size were freshly cleaved immediately before *in situ* AFM observations as well as prior to *ex situ* growth tests using dispersions of ACC nanoparticles (see below). Also, for *ex situ* batch tests using saturated $Ca(OH)_2$ solutions, as well as for growth tests using dispersions of ACC nanoparticles, optical quality calcite crystals were grounded in an agate mortar and sieved to obtain crystals with size 0.5−25 μm. To ensure statistical significance all tests/experiments and analyses were performer in triplicate (at least).

AFM Imaging Using a Fluid Cell. *In situ* observations and measurements were performed using a Digital Instruments Nanoscope III Multimode AFM (unless indicated) equipped with a fluid cell and working in contact mode under ambient conditions (T = 20 ± 1 °C). The solutions (2 mL of saturated $Ca(OH)_2$ solution with or without 60 μg/mL PAA) were injected from a syringe coupled to an O-ring-sealed fluid cell containing the sample crystal. AFM images were collected using fresh Si_3N_4 tips (Veeco Instruments, tip model NP-S20) and analyzed with Nanoscope software (version 1.40). The reported AFM tip geometry effect which results in an apparent enlargement of x/y dimensions was corrected using the methodology described in Lupulescu and Rimer.[37]

The dependence of calcite growth rates on $\sigma_{calcite}$ was evaluated using growth solutions (prepared using analytical grade $CaCl_2{\cdot}2H_2O$ and Na_2CO_3; Sigma-Aldrich) with $\sigma_{calcite}$ equal to 3.56, 4.72, 4.81, and 5.87. The first $\sigma_{calcite}$ value corresponds to the highest reported value for calcite growth (via step spreading) in AFM;[16] the second corresponds to the calculated solubility of anhydrous ACC.[8] The third value corresponds to the solubility of ACC reported by Brečević and Nielsen,[21] and the fourth one corresponds to the solubility of ACC reported by Clarkson et al.[38] No concentrations with $\sigma_{calcite} \geq$ 4.81 could be tested in the AFM because upon mixing of the reactant solutions ($CaCl_2$ and Na_2CO_3) precipitation of ACC took place immediately. Growth rates, v ($v = (v_+ + v_-)/2$, where v_+ and v_- are the speed of advancement (nm/s) of obtuse and acute steps, respectively) were determined by measuring step displacement between sequential images (typical elapsed time, $t \sim 80 \pm 7$ s). Figure S2c shows v values determined here, along with values determined by Teng et al.[39] for lower $\sigma_{calcite}$. Note that, at very high σ, normal or continuous crystal growth by direct ion/molecule incorporation into an atomically rough surface (with a high kink density) occurs in melts or from vapors; however, it is very rare in solution.[1,40] Indeed, we did not observe the latter growth mechanism, not even at the highest σ tested.

As stated above, growth solutions with $\sigma_{calcite} \geq 4.81$ led to the immediate precipitation of ACC within the injection system of the AFM fluid cell, thereby preventing the acquisition of any image (i.e., the laser used to determine the position of the cantilever was scattered by the nanoparticles deposited onto the cantilever). Similarly, direct dosing of aqueous ACC nanoparticles dispersions to the AFM fluid cell resulted in deposition of ACC onto the cantilever, an effect that is especially fastidious during the first 10−30 min after injection, and which prevented *in situ* imaging of calcite growth via ACC nanoparticle attachment. This critical problem was bypassed here using a modified version of the so-called "limewater" consolidation method, that relies on the application of a saturated $Ca(OH)_2$ solution to the surface of degraded limestone or marble, with the aim of generating new calcium carbonate cement (primarily formed via carbonation of the limewater solution in contact with atmospheric CO_2).[41] Injection of the saturated $Ca(OH)_2$ solution into the AFM fluid cell where a freshly cleaved calcite crystal was placed led to the immediate formation of a layer of ACC nanoparticles which eventually blanketed the exposed $(10.4)_{calcite}$ cleavage faces.

Prior to *in situ* AFM growth experiments, the surface of calcite crystals placed in the fluid cell was washed with 5 mL of double deionized water to eliminate any possible contaminant or surface inhomogeneity, as well as to adjust the working parameters. Flushing with water led to the development of rhombohedral dissolution pits and their spreading via step retreat, as previously reported.[42] After this initial dissolution process, the saturated $Ca(OH)_2$ solution (2 mL, with or without PAA) was injected into the fluid cell. Therefore, all AFM images labeled "Before solution injection" show rhombohedral dissolution pits (Figures 2a,c and 5). Note that injection of water did not lead to the formation of any precipitate(s) that could affect structures developed during the growth tests. Note also that *in situ* AFM analyses of the (chemi)adsorption of PAA (using aqueous solutions with varying PAA concentrations) show that scattered surface precipitates (PAA-calcium salts) can form on the calcite surface.[43] Following injection of 60 μg/mL PAA solutions (pH 9), precipitates appear as scattered, randomly distributed globules (surface density ~3 globules/μm^2), ~250 nm wide and 40−60 nm high, that tended to develop spider-web features upon dissolution with water.[43] Considering that our experiments using saturated $Ca(OH)_2$ solutions were performed at a higher pH (12.4), we tested the effects of a 60 μg/mL PAA aqueous solution whose pH was adjusted to ~12 (adding NaOH) on the dissolution of calcite. *In situ* AFM experiments show that upon solution injection the $(10.4)_{calcite}$ surface experienced dissolution via the retreat of jagged steps (Figure S18). Step pinning due to adsorption of PAA on the calcite surface was likely responsible for such a jagging of steps. After contact with the solution for more than 15−30 min, scattered precipitates (presumed to be PAA-Ca), ~300 nm wide and ~4 nm high, formed on the calcite surface (Figure S19). These textural features, however, were not observed in our *in situ* AFM experiments when $Ca(OH)_2$ solutions dosed with 60 μg/mL PAA were used.

The dissolution in water (double-deionized Milli-Q water, resistivity > 18 mΩ) of the ACC overgrowth that formed after injection of the saturated $Ca(OH)_2$ solution into the AFM fluid cell was also studied using *in situ* AFM. Ten minutes after the formation of the ACC overgrowth on $(10.4)_{calcite}$, the AFM fluid cell was flushed with 5 mL of water, and images were collected.

PHREEQC Computer Modeling. Calculation using PHREEQC and the phreeqc.dat database[44] of the (super/under)saturation with

DOI: 10.1021/acs.cgd.5b01180
Cryst. Growth Des. 2016, 16, 1850−1860

respect to calcite and ACC phases (both hydrated and anhydrous ACC) of the fluid in contact with the exposed calcite surface area assuming equilibration within the whole fluid volume (38 μL) once a calcite crystal with size 4 × 3 × 1 mm^3 was placed in the fluid cell systematically yielded a solution saturated with respect to calcite, but undersaturated with respect to any ACC phase. This was not consistent with the observed formation of an ACC precipitate. We thus considered that kinetic factors could be responsible for this effect. Because the carbonate-free saturated $Ca(OH)_2$ solution is undersaturated with respect to calcite, upon contact of this solution with the calcite crystal dissolution of up to a few monolayers of $CaCO_3$ occurs, and the CO_3^{2-} ions released at the calcite−solution interface diffuse toward the bulk solution (where the nominal $[CO_3^{2-}]$ would be zero at $t = 0$). However, the lower diffusion coefficient D, of carbonate ions in aqueous solution (0.7×10^{-9} m^2 s^{-1} at 20 °C) compared to H_2O molecules (2.01×10^{-9} m^2 s^{-1} at 20 °C),[45] and the existence of abundant free Ca ions (15.73 mM) along with the high pH (12.4) of the saturated $Ca(OH)_2$ solution, make it possible that, within a thin fluid boundary layer in contact with the calcite surface, sufficient carbonate and calcium concentrations can be reached to enable ACC precipitation if diffusion of these ions into the bulk is slow compared to the kinetics of ACC precipitation. With these assumptions, we calculated the supersaturation σ_{ACC} of such a layer with respect to ACC as a function of the thickness of this boundary layer (for the initial situation after calcite dissolution). PHREEQC computer simulations show that within a boundary layer ≤12 μm thick (solution volume of 0.13 μL with a $CaCO_3$ amount of 2.441×10^{-10} moles, surrounding a calcite crystal 4 × 3 × 1 mm in size,), a $\sigma_{ACC} > 0$ can be reached (for hydrated ACC with $k_{sp,ACC} = 10^{-6.39}$),[21] thereby enabling hydrated ACC precipitation, as observed experimentally. Simulations show that the thinner the boundary layer is, the higher the value of σ_{ACC} is (up to a limiting value of ca. 40 nm, corresponding to the average thickness of the attached ACC layer) (Figure 1). However, the very small amount of calcite dissolved (i.e., a total of 2.441×10^{-10} moles of calcite can dissolve in the 38 μL free volume of the fluid cell) would preclude the precipitation of a large amount of ACC. This helps to explain why our AFM and FESEM observations show that, in general, the ACC overgrowth is made up of a monolayer or, in some cases, up to a few layers, with some scattered particles on top. In contrast, multilayer growth is typically observed in the case of calcite growth via addition of ACC nanoparticle dispersions (see experimental details below) because a larger amount of ACC nanoparticles is administered.

***Ex Situ* Calcite Growth Tests Using Saturated $Ca(OH)_2$ Solutions.** Calcite crystals with size 0.5−25 μm (ca. 100 mg) were placed in Teflon batch reactors at 20 °C where 100 mL of saturated $Ca(OH)_2$ solution (with or without 60 μg/mL PAA) was added. Special care was taken to avoid contact of the solution with atmospheric CO_2 in order to prevent undesired carbonation. At predefined time intervals (1 min, 2 min, 22 min, 2 h), dispersions were collected and immediately vacuum-filtered. Solids were subsequently dried at room T and stored under dry conditions for further analysis.

ACC Synthesis and Calcite Growth Using ACC Nanoparticle Dispersions. ACC nanoparticles were synthesized by mixing 100 mM $CaCl_2$ and 100 mM Na_2CO_3 aqueous solutions under vigorous stirring at room T in the absence or in the presence of 60 μg/mL PAA. Upon ACC precipitation, the solids were separated by centrifugation (10 min, 5000 rpm; Kubota KS-8000) and dispersed in isopropanol (Panreac, absolute PRS) for stabilization (i.e., prevention of ACC-to-crystalline transformation) prior to further analysis/test. ACC nanoparticles were characterized by X-ray diffraction (XRD), Fourier transform infrared spectroscopy (FTIR), thermogravimetry/differential scanning calorimetry (TG/DSC), and transmission electron microscopy (TEM) coupled with selected area electron diffraction (SAED) (see details below). Analyses show that ACC is stable for over 1 month when stored in isopropanol (Figure S11). From the stock ACC alcohol dispersions, aliquots were collected, and dispersed in freshly prepared aqueous solutions saturated with respect to ACC (solid mass fraction ca. 0.002−0.004), and droplets (10 μL) of aqueous ACC dispersions were deposited onto freshly cleaved optical quality calcite crystals, as well as on calcite powders, dried at room T and stored either in a desiccator at low RH (silica gel) or in a closed container at high RH (85%). The latter storage condition was selected to facilitate ACC-to-calcite transformation via dissolution/precipitation.[8] Samples were collected after 72 h storage for further analysis using field emission scanning electron microscopy (FESEM) (powders and crystals) and TEM (powders). Note that for these analyses we choose to use powdered calcite as support (as opposed to the single crystals used in AFM experiments) in order to obtain samples that could readily be used for TEM observations. To evaluate the effect of the composition and structure of the substrate (crystalline vs amorphous) on the deposition and self-assembly of ACC nanoparticles, control experiments were performed using an amorphous substrate (silica glass slides) as well as crystalline ultraclean [100]-oriented silicon wafers (Virginia Semiconductor Inc.) and quartz crystals. For this task, ACC nanoparticle dispersion droplets were deposited onto these substrates and subjected to similar storing conditions and analyses as described above for the case of ACC nanoparticle dispersion droplets deposited on calcite.

The zeta-potential of ACC nanoparticles (formed in the presence and absence of PAA) was determined on a Malvern Zetasizer Nano ZS apparatus (Malvern Instruments) at 21 °C using aqueous dispersion of freshly precipitated ACC.

The pH of the nanoparticle dispersions was 9.6 ± 0.2, a value lower than that of the saturated $Ca(OH)_2$ solution (pH 12.4). Such a pH difference, however, does not seem to affect the experimental results. AFM, FESEM, and TEM analyses show that the textural features of ACC overgrowths and calcite formed after ACC-to-crystalline transformation were very similar in both cases.

***Ex Situ* TG/DSC, XRD, FTIR, and FESEM Analyses.** XRD analysis of calcite crystals (prior and after ACC-induced growth) and homogeneously synthesized ACC nanoparticles was performed on a Philips X'Pert Pro X-ray diffractometer equipped with Cu Kα radiation (λ = 1.5405 Å) at 2θ range between 3° and 60° and at a scanning rate of 0.002° 2θ/s.

Solids collected at different time intervals during *ex situ* batch reactor experiments (growth in $Ca(OH)_2$ saturated solutions) as well as homogeneously synthesized ACC nanoparticles were subjected to simultaneous TG/DSC analysis on a Mettler-Toledo model TGA/DSC1. About 10−20 mg of sample was deposited on Pt crucibles and analyzed under flowing air (100 mL/min) at 20 °C/min heating rate, from 25 to 950 °C. Solids were also analyzed on a JASCO 6200 FTIR (frequency range 400−4000 cm^{-1}; 4 cm^{-1} spectral resolution) equipped with an attenuated total reflectance (ATR) device for spectra collection without sample preparation (i.e., minimizing artifacts such as dehydration of ACC).

The surface area (BET method) of solids collected at different time intervals during *ex situ* batch reactor experiments (growth in $Ca(OH)_2$ saturated solutions) as well as homogeneously synthesized ACC nanoparticles was determined by means of N_2 adsorption at 77 K on a Micromeritics TriStar 3000, following degassing for 2 h at 60 °C under vacuum on a Micromeritics FlowPrep device.

Analysis of calcite substrates and ACC overgrowths developed during batch reactor tests (saturated $Ca(OH)_2$ solutions) and ACC dispersion droplet tests, as well as homogeneously synthesized ACC, was performed by means of TEM using a FEI Titan, operated at 300 kV. Powder samples were dispersed in ethanol, sonicated for 30 s, and fished with holey Formvar C-coated Cu grids. TEM observations were performed using a 30 μm objective aperture. SAED patterns were collected using a 10 μm aperture, which allowed collection of diffraction data from a circular area ca. 0.2 μm in diameter. Bright field images and SAED patterns were collected first. Then, lattice images (HRTEM) were rapidly collected to minimize beam damage. Line-scanning C and Ca compositional analyses were performed along profiles including the calcite substrate and the ACC overgrowth using the annular dark-field scanning TEM (STEM) mode.

Solids were also observed at high magnification using a scanning electron microscope equipped with a field emission gun (FESEM Zeiss SUPRA40VP). Samples were carbon coated prior to FESEM observation. Comparison of the nanotextural features of ACC

DOI: 10.1021/acs.cgd.5b01180
Cryst. Growth Des. 2016, 16, 1850−1860

overgrowths in images collected using FESEM (or TEM) with those collected *in situ* using the AFM show that sample preparation for FESEM (or TEM) did not add any apparent drying artifact.

■ ASSOCIATED CONTENT

Supporting Information

The Supporting Information is available free of charge on the ACS Publications website at DOI: 10.1021/acs.cgd.5b01180.

Additional figures, including AFM images and TEM and FESEM photomicrographcs (PDF)

■ AUTHOR INFORMATION

Corresponding Author

*E-mail: carlosrn@ugr.es. Phone: +34 958 246616.

Author Contributions

The manuscript was written through the contributions of all authors.

Notes

The authors declare no competing financial interest.

■ ACKNOWLEDGMENTS

This work was financially supported by the Spanish Government (Grants MAT2012-37584, CGL2012-35992, and CGL2015-70642-R) and the Junta de Andalucía (Research Group RNM-179 and Project P11-RNM-7550). E.R.-A. acknowledges a Ramón y Cajal grant. We thank the Centro de Instrumentación Científica (CIC; University of Granada) for analytical assistance. C.V.P. acknowledges funding from the EU Marie Curie initial training networks, Minsc and CO_2React. We thank A. Checa for the FESEM images of seminacre. We also thank M. A. Fenner from KeySight Technologies for the *in situ* AFM image shown in Figure S13, which was collected using an Agilent 7500 AFM equipped with a fluid cell.

■ REFERENCES

(1) Chernov, A. A. *Modern Crystallography III*; Springer: Berlin, 1984.

(2) Meldrum, F.; Cölfen, H. Controlling mineral morphologies and structures in biological and synthetic systems. *Chem. Rev.* **2008**, *108*, 4332−4432.

(3) De Yoreo, J. J.; Gilbert, P. U. P. A.; Sommerdijk, N. A. J. M.; Penn, R. L.; Whitelam, S.; Joester, D.; Zhang, H.; Rimer, J. D.; Navrotsky, A.; Banfield, J. F.; Wallace, A. F.; Michel, F. M.; Meldrum, F. C.; Cölfen, H.; Dove, P. M. Crystallization by particle attachment in synthetic, biogenic, and geologic environments. *Science* **2015**, *349*, 498.

(4) Nielsen, M. H.; Aloni, S.; De Yoreo, J. J. In situ TEM imaging of $CaCO_3$ nucleation reveals coexistence of direct and indirect pathways. *Science* **2014**, *345*, 1158−1162.

(5) Pouget, E. M.; Bomans, P. H. H.; Goos, J.; Frederik, P. M.; de With, G.; Sommerdijk, N. A. J. M. The initial stages of template-controlled $CaCO_3$ formation revealed by cryo-TEM. *Science* **2009**, *323*, 1455−1458.

(6) Gebauer, D.; Völkel, A.; Cölfen, H. Stable prenucleation clusters. *Science* **2008**, *322*, 1819−1822.

(7) Wallace, A. F.; Hedges, L. O.; Fernandez-Martinez, A.; Raiteri, P.; Gale, J. D.; Waychunas, G. A.; Whitelam, S.; Banfield, J. F.; De Yoreo, J. J. Microscopic evidence for liquid-liquid separation in supersaturated $CaCO_3$ solutions. *Science* **2013**, *341*, 885−889.

(8) Rodriguez-Navarro, C.; Kudlacz, K.; Cizer, Ö.; Ruiz-Agudo, E. Formation of amorphous calcium carbonate and its transformation into mesostructured calcite. *CrystEngComm* **2015**, *17*, 58−72.

(9) Addadi, L.; Raz, S.; Weiner, S. Taking advantage of disorder: Amorphous calcium carbonate and its roles in biomineralization. *Adv. Mater.* **2003**, *15*, 959−970.

(10) Politi, Y.; Metzler, R. A.; Abrecht, M.; Gilbert, B.; Wilt, F. H.; Sagi, I.; Addadi, L.; Weiner, S.; Gilbert, P. U. P. A. Transformation mechanisms of amorphous calcium carbonate into calcite in the sea urchin larval spicule. *Proc. Natl. Acad. Sci. U. S. A.* **2008**, *105*, 17362−17366.

(11) Radha, A. V.; Forbes, T. Z.; Killian, C. E.; Gilbert, P. U. P. A.; Navrotsky, A. Transformation and crystallization energetics of synthetic and biogenic amorphous calcium carbonate. *Proc. Natl. Acad. Sci. U. S. A.* **2010**, *107*, 16438−16443.

(12) Vidavsky, N.; Addadi, S.; Mahamid, J.; Shimoni, E.; Ben-Ezra, D.; Shpigel, M.; Weiner, S.; Addadi, L. Initial stages of calcium uptake and mineral deposition in sea urchin embryos. *Proc. Natl. Acad. Sci. U. S. A.* **2014**, *111*, 39−44.

(13) Song, R. Q.; Cölfen, H.; Xu, A. W.; Hartmann, J.; Antonietti, M. Polyelectrolyte-directed nanoparticle aggregation: Systematic morphogenesis of calcium carbonate by nonclassical crystallization. *ACS Nano* **2009**, *3*, 1966−1978.

(14) Gal, A.; Weiner, S.; Addadi, L. A perspective on underlying crystal growth mechanisms in biomineralization: solution mediated growth versus nanosphere particle accretion. *CrystEngComm* **2015**, *17*, 2606−2615.

(15) Gal, A.; Kahil, K.; Vidavsky, N.; DeVol, R. L.; Gilbert, P. U. P. A.; Fratzl, P.; Weiner, S.; Addadi, L. Particle accretion mechanism underlies biological crystal growth from an amorphous precursor phase. *Adv. Funct. Mater.* **2014**, *24*, 5420−5426.

(16) Sethmann, I.; Putnis, A.; Grassmann, O.; Löbmann, P. Observation of nano-clustered calcite growth via a transient phase mediated by organic polyanions: A close match for biomineralization. *Am. Mineral.* **2005**, *90*, 1213−1217.

(17) Sethmann, I.; Hinrichs, R.; Wörheide, G.; Putnis, A. Nano-cluster composite structure of calcitic sponge spicules - a case study of basic characteristics of biominerals. *J. Inorg. Biochem.* **2006**, *100*, 88−96.

(18) Burton, W. K.; Cabrera, N.; Frank, F. C. The growth of crystals and the equilibrium structure of their surfaces. *Philos. Trans. R. Soc., A* **1951**, *243*, 299−358.

(19) Teng, H.; Dove, P. M.; Orme, C.; De Yoreo, J. J. Thermodynamics of calcite growth: baseline for understanding biomineral formation. *Science* **1998**, *282*, 724−727.

(20) Gower, L. B. Biomimetic model systems for investigating the amorphous precursor pathway and its role in biomineralization. *Chem. Rev.* **2008**, *108*, 4551−4627.

(21) Brečević, L.; Nielsen, A. E. Solubility of amorphous calcium carbonate. *J. Cryst. Growth* **1989**, *98*, 504−510.

(22) Xu, X.; Han, J. T.; Cho, K. Deposition of amorphous calcium carbonate hemispheres on substrates. *Langmuir* **2005**, *21*, 4801−4804.

(23) Smeets, P. J. M.; Cho, K. R.; Kempen, R. G. E.; Sommerdijk, N. A. J. M.; De Yoreo, J. J. Calcium carbonate nucleation driven by ion binding in a biomimetic matrix revealed by *in situ* electron microscopy. *Nat. Mater.* **2015**, *14*, 394−399.

(24) Krinke, T. J.; Fissan, H.; Deppert, K. Deposition of aerosol nanoparticles on flat substrate surfaces. *Phase Transitions* **2003**, *76*, 333−345.

(25) Gebauer, D.; Kellermeier, M.; Gale, J. D.; Bergström, L.; Cölfen, H. Pre-nucleation clusters as solute precursors in crystallisation. *Chem. Soc. Rev.* **2014**, *43*, 2348−2371.

(26) Ganapathy, R.; Buckley, M. R.; Gerbode, S. J.; Cohen, I. Direct measurements of island growth and step-edge barriers in colloidal epitaxy. *Science* **2010**, *327*, 445−448.

(27) Imada, H.; Kimura, K.; Onishi, H. Water and 2-propanol structured on calcite (104) probed by frequency-modulation atomic force microscopy. *Langmuir* **2013**, *29*, 10744−10751.

(28) Zhang, H.; De Yoreo, J. J.; Banfield, J. F. A unified description of attachment-based crystal growth. *ACS Nano* **2014**, *8*, 6526−6530.

(29) Gebauer, D.; Gunawidjaja, P. N.; Ko, J. Y. P.; Bacsik, Z.; Aziz, B.; Liu, L. J.; Hu, Y. F.; Bergström, L.; Tai, C. W.; Sham, T. K.; Edén, M.; Hedin, N. Proto-calcite and proto-vaterite in amorphous calcium carbonates. *Angew. Chem., Int. Ed.* **2010**, *49*, 8889−8891.

DOI: 10.1021/acs.cgd.5b01180
Cryst. Growth Des. 2016, 16, 1850−1860

(30) Kim, Y.-Y.; Schenk, A. S.; Ihli, J.; Kulak, A. N.; Hetherington, N. B. J.; Tang, C. C.; Schmahl, W. W.; Griesshaber, E.; Hyett, G.; Meldrum, F. C. A Critical analysis of calcium carbonate mesocrystals. *Nat. Commun.* **2014**, *5*, 4341.
(31) Yang, L.; Killian, C. E.; Kunz, M.; Tamura, N.; Gilbert, P. U. P. A. Biomineral nanoparticles are space-filling. *Nanoscale* **2011**, *3*, 603−609.
(32) Putnis, A. Why mineral interfaces matter. *Science* **2014**, *343*, 1441−1442.
(33) Putnis, A. Mineral replacement reactions. *Rev. Mineral. Geochem.* **2009**, *70*, 87−124.
(34) Mullin, J. W. *Crystallization*, 4th ed.; Butterworth: London, 2001.
(35) Rodriguez-Navarro, A. B.; Marie, P.; Nys, Y.; Hincke, M. T.; Gautron, J. Amorphous calcium carbonate controls avian eggshell mineralization: A new paradigm for understanding rapid eggshell calcification. *J. Struct. Biol.* **2015**, *190*, 291−303.
(36) Mahamid, J.; Sharir, A.; Addadi, L.; Weiner, S. Amorphous calcium phosphate is a major component of the forming fin bones of zebrafish: Indications for an amorphous precursor phase. *Proc. Natl. Acad. Sci. U. S. A.* **2008**, *105*, 12748−12753.
(37) Lupulescu, A. I.; Rimer, J. D. In situ imaging of silicalite-1 surface growth reveals the mechanism of crystallisation. *Science* **2014**, *344*, 729−732.
(38) Clarkson, J. R.; Price, T. J.; Adams, C. J. Role of metastable phases in the spontaneous precipitation of calcium carbonate. *J. Chem. Soc., Faraday Trans.* **1992**, *88*, 243−249.
(39) Teng, H. H.; Dove, P. M.; De Yoreo, J. J. Kinetics of calcite growth: surface processes and relationships to macroscopic rate laws. *Geochim. Cosmochim. Acta* **2000**, *64*, 2255−2266.
(40) Malkin, A. J.; Kuznetsov, Y. G.; Land, T. A.; De Yoreo, J. J.; McPherson, A. Mechanisms of growth for proteins and virus crystals. *Nat. Struct. Biol.* **1995**, *2*, 956−959.
(41) Brajer, I.; Kalsbeek, N. Limewater absorption and calcite crystal formation on a limewater-impregnated secco wall painting. *Stud. Conserv.* **1999**, *44*, 145−156.
(42) Ruiz-Agudo, E.; Putnis, C. V. Direct observations of mineral−fluid reactions using atomic force microscopy: the specific example of calcite. *Mineral. Mag.* **2012**, *76*, 227−253.
(43) Mureşan, L.; Sinha, P.; Maroni, P.; Borkovec, M. Adsorption and surface-induced precipitation of poly(acrylic acid) on calcite revealed with atomic force microscopy. *Colloids Surf., A* **2011**, *390*, 225−230.
(44) Parkhurst, D. L.; Appelo, C. A. J. *User Guide to PHREEQC (version 2)—A Computer Program for Speciation, Batch Reaction, One Dimensional Transport, and Inverse Geochemical Calculations.* U.S. Geological Survey Water-Resources Investigation Report 99-4259; Denver, Colorado, 1999.
(45) Zeebe, R. E. On the molecular diffusion coefficients of dissolved CO_2, HCO_3^-, and CO_3^{2-} and their dependence on isotopic mass. *Geochim. Cosmochim. Acta* **2011**, *75*, 2483−2498.

DOI: 10.1021/acs.cgd.5b01180
Cryst. Growth Des. 2016, 16, 1850−1860